

An Open-source Bayesian Atmospheric Radiative Transfer (BART) Code: II. The TRANSIT Radiative-Transfer Module and Retrieval of HAT-P-11b

Patricio E. Cubillos^{1,2}, Joseph Harrington², Jasmina Blečić^{3,2}, Michael D. Himes², Patricio M. Rojo⁴, Thomas J. Loredo⁵, Nate B. Lust^{2,6}, Ryan C. Challener², Austin J. Foster², Madison M. Stemm², Andrew S. D. Foster^{2,5}, and Sarah D. Blumenthal^{2,7}

¹Space Research Institute, Austrian Academy of Sciences, Schmiedlstrasse 6, A-8042 Graz, Austria

²Planetary Sciences Group, Department of Physics, University of Central Florida, Orlando, FL 32816-2385, USA

³Department of Physics, New York University Abu Dhabi, PO Box 129188 Abu Dhabi, UAE.

⁴Departamento de Astronomía, Universidad de Chile, Camino del Observatorio, 1515 Las Condes, Santiago, Chile

⁵Cornell Center for Astrophysics and Planetary Sciences, Space Sciences Building, Cornell University, Ithaca, NY 14853-6801, USA

⁶Department of Astrophysical Sciences, Princeton University, Princeton, NJ 08544, USA

⁷Department of Physics, University of Oxford, Oxford OX1 3PU, UK

Abstract

This and companion papers by Harrington et al. and Blečić et al. present the Bayesian Atmospheric Radiative Transfer (BART) code, an open-source, open-development package to characterize extrasolar-planet atmospheres. BART combines a thermochemical equilibrium abundances (TEA), a radiative-transfer (TRANSIT), and a Bayesian statistical (MC3) module to constrain atmospheric temperatures and molecular abundances for given spectroscopic observations. Here, we describe the TRANSIT radiative-transfer package, an efficient line-by-line radiative-transfer C code for one-dimensional atmospheres, developed by P. Rojo and further modified by the UCF exoplanet group. This code produces transmission and hemisphere-integrated emission spectra. TRANSIT handles line-by-line opacities from HITRAN, Partridge & Schwenke (H₂O), Schwenke (TiO), and Plez (VO); and collision-induced absorption from Borysow, HITRAN, and ExoMol. TRANSIT emission-spectra models agree with models from C. Morley (priv. comm.) within a few percent. We applied BART to the *Spitzer* and *Hubble* transit observations of the Neptune-sized planet HAT-P-11b. Our analysis of the combined *HST* and *Spitzer* data generally agrees with those from previous studies, finding atmospheric models with enhanced metallicity ($\gtrsim 100\times$ solar) and high-altitude clouds ($\lesssim 1$ mbar level). When analyzing only the *HST* data, our models favor high-metallicity atmospheres, in contrast with the previous analysis by Chachan et al. We suspect that this discrepancy arises from the different choice of chemistry modeling (free constant-with-altitude vs. thermochemical equilibrium) and the enhanced parameter correlations found when neglecting the *Spitzer* observations. The BART source code and documentation are available at <https://github.com/exosports/BART>.

Unified Astronomy Thesaurus concepts: Planetary atmospheres (1244); Exoplanet atmospheric composition (2021); Astrostatistics techniques (1886); Open source software (1866)

1. Introduction

Transiting exoplanets are some of the most valuable targets for the study of planetary atmospheres, since they provide a much more diverse range of physical properties than that found in the solar-system planets. Photometric time-series observations when a planet passes in front (transits) of its host star constrain the size of the exoplanet; whereas observations when a planet passes behind (eclipse) constrain the light emitted and reflected by the planet. If the planetary mass is also known, these observations allow us to estimate the bulk density, gravity, and temperature of the planet's atmosphere. Furthermore, spectroscopic transit or eclipse observations trace the transmission or emission spectral variations imprinted by the atmospheric species, respectively.

Since each species in a planet's atmosphere produces a specific absorption and emission pattern (at a given temperature and pressure), with enough spectral resolution and coverage one can constrain the composition of the exoplanetary atmosphere.

Numerous physical processes can shape the temperature and composition of an atmosphere, ranging from formation scenarios (e.g., Öberg et al. 2011; Drummond et al. 2019); equilibrium-chemistry, photochemistry, kinetics (e.g., Moses et al. 2013; Madhusudhan et al. 2016); circulation dynamics (e.g., Showman et al. 2009; Mayne et al. 2014); to cloud physics (e.g., Marley et al. 2013; Morley et al. 2015). However, once the properties of an atmosphere are known or assumed (i.e., the pressure, temperature, and composition), the radiative-transfer equation ultimately relates the atmospheric state to the observed spectrum.

Corresponding author: Patricio Cubillos
patricio.cubillos@oew.ac.at

Radiative-transfer calculations for exoplanet atmospheres need to deal with a wide range of challenges, including limited laboratory or theoretical opacity data at high temperatures (Fortney *et al.* 2016), oversimplified atmospheric models (e.g., Rocchetto *et al.* 2016; Caldas *et al.* 2019; Taylor *et al.* 2020), or stellar contamination (Rackham *et al.* 2018).

Radiative transfer models for substellar-object atmospheres have been continuously developed for decades, with early exoplanet models naturally building upon the previous experience from Solar System planets and brown dwarfs (e.g., McKay *et al.* 1989; Marley *et al.* 1996; Oppenheimer *et al.* 1998; Burrows *et al.* 1997). Consequently, to date there are a large number of models, varying in complexity and focus, from 1D (e.g., Burrows *et al.* 2005; Fortney 2005; Seager *et al.* 2005) to 3D (e.g., Fortney *et al.* 2010), or focused on infrared (e.g., Dudhia 2017) or optical wavelengths (e.g., Lupu *et al.* 2016).

The limited signal-to-noise ratio, spectral resolution, and spectral coverage of exoplanet data generally leads to poorly constrained and degenerate constraints of the atmospheric properties. This has led to the development of high-performance radiative-transfer codes (e.g., Waldmann *et al.* 2015; Kempton *et al.* 2017; Malik *et al.* 2017) and statistically-robust Bayesian retrieval frameworks (e.g., Madhusudhan & Seager 2010; Benneke & Seager 2012; Line *et al.* 2013; Waldmann *et al.* 2015; Lavie *et al.* 2017; Lupu *et al.* 2016; Barstow *et al.* 2017; Evans *et al.* 2017; MacDonald & Madhusudhan 2017; Gandhi & Madhusudhan 2018; Mollière *et al.* 2019; Zhang *et al.* 2019; Lothringer & Barman 2020; Min *et al.* 2020; Cubillos & Blečić 2021)—some of which are available as open-source software. A Bayesian retrieval is the most appropriate approach when fitting poorly-constrained models. This approach explores the parameter space by evaluating a large number of models. Here, the data drive the exploration towards the most-probable solutions, guided by the likelihood function and priors. The data quality determines the span of the highest-probability-density credible region of the model parameters (i.e., the error bars) and quantify any correlations. Weakly constraining data produce large model parameter uncertainties.

Nowadays, exoplanet atmospheric characterization is developing at a thrilling pace. The combined observations from ground-based, *Spitzer*, and *Hubble* telescopes create a high demand for interpretation of the data. Furthermore, the *James Webb Space Telescope (JWST)* (Gardner *et al.* 2006) will continue this trend, allowing for exoplanet characterization with unprecedented detail. The limited 5–10 year mission duration *JWST*, will require prompt modeling of the data, hopefully from multiple, independent teams. Having a range of retrieval frameworks readily available benefits the community by facilitating preparatory and inter-comparison studies to fully exploit the constraining power of present and future instrumentation.

1.1. The Bayesian Atmospheric Radiative-Transfer Package

In this context, we developed the open-source Bayesian Atmospheric Radiative Transfer (BART) package for statis-

tically robust exoplanet characterization, which we present jointly in three articles. Harrington *et al.* (2021, submitted) presents an overview of the retrieval framework, testing, and an application to the eclipse data of HD 189733 b. This article focuses on the radiative-transfer module, with an application to the transit data of HAT-P-11b. Blečić *et al.* (2021, submitted) focuses on the initialization and post-processing routines, with an application to the eclipse data of WASP-43b. BART offers both forward-model and retrieval tools to model exoplanet spectra and constrain the atmospheric temperature and composition. BART is an open-development project available under the Reproducible Research Software License (see Harrington *et al.* 2021). The code repositories and documentation are available under version control at <https://github.com/exosports/BART>.

BART combines three general-purpose and independent sub-packages. The Thermochemical Equilibrium Abundances code (TEA, Blečić *et al.* 2016) computes mole mixing ratios (abundances) of atmospheric species under thermochemical equilibrium. Thus, TEA can provide an initial guess for the atmospheric abundances to the BART framework. The radiative-transfer package, TRANSIT, computes line-by-line transmission or emission spectra for given one-dimensional atmospheric models. The Multi-Core Markov-Chain Monte Carlo statistical package (MC3, Cubillos *et al.* 2017) is a general-purpose, model-fitting package that provides parallel multiprocessor Markov-chain Monte Carlo (MCMC) to explore the parameter space. MC3 implements the snooker Differential-evolution MCMC algorithm (DEMC, ter Braak 2006; ter Braak & Vrugt 2008).

This paper is organized as follows: section 2 details the radiative-transfer calculation, its assumptions, geometry treatment, available data bases, and validation tests. Section 3 shows our retrieval analysis of the extrasolar planet HAT-P-11b using BART. Finally, Section 4 presents our prospects for the BART project and summarizes our conclusions.

2. The TRANSIT Radiative-transfer Package

Here we describe the treatment of the radiative-transfer equation in the TRANSIT code, which is generally based on Andrews (2000) and Rybicki & Lightman (1986). The radiative-transfer equation describes how light propagates as it travels through a medium. Let the specific intensity, I_ν , denote the power carried by rays per unit area, dA , per unit wavenumber, ν , in the interval $d\nu$, within a solid angle $d\Omega$. Then, the radiative-transfer equation for the specific intensity is given by:

$$\frac{dI_\nu}{ds} = -e_\nu(I_\nu - S_\nu), \quad (1)$$

where s is the path traveled by the light ray, e_ν is the extinction coefficient, and S_ν is the source function. The extinction depends on the atmospheric composition, pressure, and temperature. The observed flux spectrum is the integral of the specific intensity multiplied by the cosine of the polar angle over the solid angle. Therefore, by solving the radiative-transfer equation for a given observing geometry

and atmospheric model, we can model the observed spectrum as a function of wavelength.

The TRANSIT package solves the one-dimensional radiative-transfer equation for two relevant cases of exoplanet observations: the transmission spectrum for transit observations, and the hemisphere-integrated emission spectrum for eclipse observations. The model assumes hydrostatic balance, local thermodynamic equilibrium, and the ideal gas law. The opacity comes from electronic, rotational, and vibrational line-transition absorptions (hereafter, simply called “line transitions”, LT), collision-induced absorption (CIA), Mie and Rayleigh scattering, bound-free and free-free transitions (e.g., H^-), and aerosols. The TRANSIT code currently implements line-transition, CIA, Rayleigh, and gray-cloud opacities.

TRANSIT is a C, modular, object-oriented code, wrapped with SWIG¹ for use in Python. The code was originally developed by Rojo (2006). We rewrote the code to be one of the core packages of the BART project, implementing the eclipse-geometry mode, and improving the overall performance. The current version of TRANSIT is an open-source project hosted at <https://github.com/exosports/transit>. The repository includes a user manual that describes the main features, inputs, and outputs of the code, and provides sample runs. A second document aimed at developers, the code manual, details the data structures and the file formats.

2.1. Transit Workflow

The TRANSIT program divides the spectrum calculation into two main steps (Fig. 1). The first step initializes the required variables, reading and processing the input files. The user can optionally create an opacity grid to avoid computing line-by-line opacities for each spectrum calculation. The second step solves the radiative-transfer equation, which involves computing the ray paths, calculating the opacity at the given pressure, temperature, and wavenumber, and producing the spectrum. This separation is intended to improve the performance of the code when run multiple times (e.g., in a MCMC). With the exception of the atmospheric profiles, none of the inputs read during the initialization change during the course of the calculations. Thus, the user can produce multiple spectrum models, updating the atmospheric model each time, without the need to reprocess the input files (which can be large, like the line transition information).

TRANSIT requires as inputs: (1) a configuration file that indicates the wavenumber sampling, observing geometry, input files, etc.; (2) a one-dimensional atmospheric model that specifies the atmospheric composition and the pressure, altitude, temperature, and species abundances of each layer; and (3) line-by-line and/or cross-section opacity files. The following sections further detail the assumptions and available opacity databases for TRANSIT.

2.2. Observing Geometry

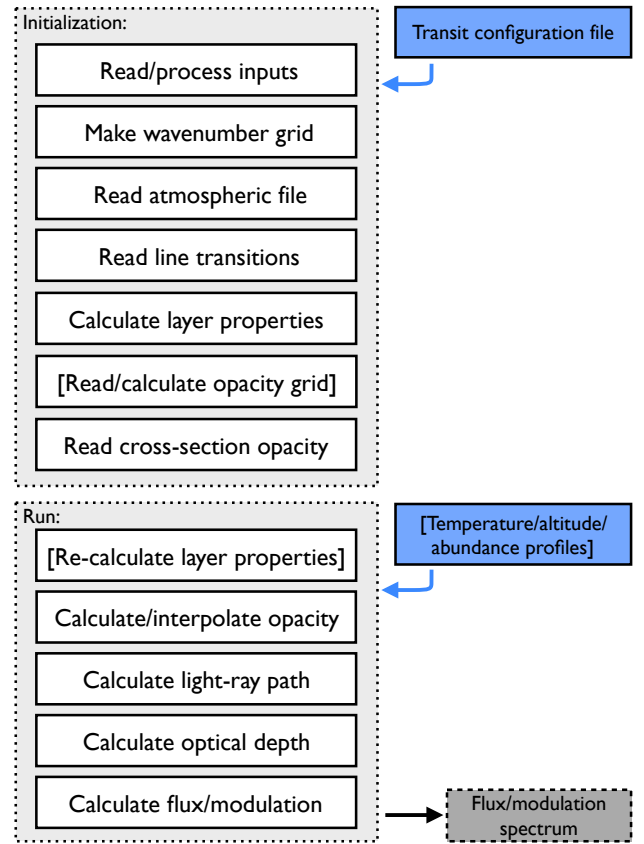


Figure 1. TRANSIT flow chart. The white boxes denote the main routines, the blue boxes the code inputs, and the gray box the output spectrum file. TRANSIT sequentially executes the routines from the top down. The items in brackets are optional steps. The execution consists of two main steps. The initialization step reads the input files, creates the (equi-spaced) wavenumber array, calculates the layer’s altitude and species density and partition function, and computes or reads a tabulated opacity grid (optional). The second main step updates the atmospheric model (if requested) and computes the atmospheric opacity over the spectral range, the light-ray path, the optical depth, and the intensity and flux spectra. Once the initialization is executed, the user can produce multiple spectrum calculations for desired atmospheric models, for example, during an MCMC the code cycles over the bottom section.

The TRANSIT code computes transmission and emission spectra, appropriate to exoplanet transit or secondary-eclipse observations, respectively. Depending on the observing geometry, the code makes different approximations about the geometry and fluxes. Much of the formulation laid out in this section is more thoroughly described in textbooks (see e.g., Seager 2010, and references therein).

2.2.1. Transit Geometry

During a transit event (Fig. 2) the planet blocks a fraction of the stellar light, which is proportional to the planet-to-star area ratio, R_p^2/R_s^2 . Since each species imprints a characteristic absorbing pattern as a function of wavelength, the planetary atmosphere modulates the transmission (or modulation) spectrum at each wavenumber ν :

$$M_\nu = \frac{F_{\nu,O} - F_{\nu,T}}{F_{\nu,O}}, \quad (2)$$

¹ swig.org/

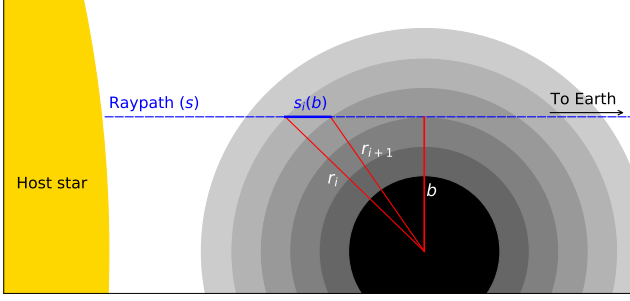


Figure 2. Transit-geometry observation diagram. The atmospheric model consists of a set of one-dimensional spherically-symmetrical shells (gray gradient) around the planet center. All the observed light rays (blue dashed line) travel nearly parallel to each other and, hence, the optical depth for each ray depends exclusively on the impact parameter (b), where the path traveled between two layers (blue solid line) is given by $s_i(b) = \sqrt{r_{i+1}^2 - b^2} - \sqrt{r_i^2 - b^2}$.

where $F_{\nu,T}$ and $F_{\nu,O}$ are the observed specific fluxes in and out of transit, respectively.

For transmission geometry, the planetary emission is small compared to the stellar intensity. Then, we can neglect the source-function term from the radiative-transfer equation. Eq. (1) then leads to:

$$\frac{dI_\nu}{ds} = -e_\nu I_\nu. \quad (3)$$

Let I_ν^0 be the stellar specific intensity. By defining the optical depth along a path, s , as:

$$\tau_\nu = \int_{\text{path}} e_\nu ds, \quad (4)$$

the solution for the transmission radiative-transfer equation becomes:

$$I_\nu = I_\nu^0 e^{-\tau_\nu}. \quad (5)$$

The specific flux in the direction of the observer, F_ν , is the integral of the first moment of the specific intensity over the solid angle, $d\Omega$:

$$F_\nu = \int I_\nu \cos\theta d\Omega, \quad (6)$$

where θ is the angle between the ray beams and the normal vector of the detector. Since the distance from Earth to the system, d , is much larger than the distance from the star to the planet, the stellar radius, and the planetary radius ($d \gg a$, $d \gg R_s$, and $d \gg R_p$, respectively), we can assume that the observed rays travel in a parallel beam thorough the planetary atmosphere. Considering an idealized star with a uniform spectrum across its surface (i.e., ignoring surface features and accounting for limb darkening in the analysis producing the transit depths) and a spherically symmetric planet, we can consider the planet centered in front of the star and rewrite the solid-angle integral as an integral over the projected disks of the planet and the star:

$$F_\nu = \frac{2\pi}{d^2} \int_0^{R_s} I_\nu r dr. \quad (7)$$

For the out-of-transit flux, Equation (7) gives:

$$F_{\nu,O} = \pi I_\nu^0 \left(\frac{R_s}{d} \right)^2. \quad (8)$$

For the in-transit flux, we assume that the planetary atmosphere is a set of spherically-symmetrical homogeneous layers (Fig. 2). Then, the optical depth becomes a function of the impact parameter of the light ray, b : $\tau_\nu = \tau_\nu(b)$. Considering now a planetary altitude, R_{top} , high enough such that $e^{-\tau_\nu(R_{\text{top}})} \approx 1$ (in practice, the top layer of the atmospheric model), we can separate the integral of Eq. (7) into the regions occulted and unocculted by the planet. Further, considering a limb-darkening-corrected transit depth, the in-transit specific flux becomes:

$$F_{\nu,T} = \frac{2\pi}{d^2} \int_0^{R_s} I_\nu^0 e^{-\tau_\nu(b)} r dr, \quad (9)$$

$$= \frac{2\pi}{d^2} I_\nu^0 \left[\int_0^{R_{\text{top}}} e^{-\tau_\nu} b db + \frac{R_s^2 - R_{\text{top}}^2}{2} \right]. \quad (10)$$

Finally, substituting Equations (8) and (10) into (2), we calculate the modulation spectrum as:

$$M_\nu = \frac{1}{R_s^2} \left[R_{\text{top}}^2 - 2 \int_0^{R_{\text{top}}} e^{-\tau_\nu} b db \right]. \quad (11)$$

2.2.2. Eclipse Geometry

An eclipse event reveals the planetary emission integrated over the day-side hemisphere. In this case, TRANSIT obtains the emerging intensity at the top of the atmospheric model by solving the radiative-transfer equation under the plane-parallel approximation. Additionally, TRANSIT adopts the local thermodynamic equilibrium approximation, where the source function becomes the Planck function $B_\nu(T)$.

Considering the vertical optical depth, $d\tau_{\nu,z} = -e_\nu dz$ (with origin $\tau = 0$ at the top of the atmosphere), the path, ds , of a ray with an angle α , with respect to the normal vector, is related to the vertical path as $ds = dz / \cos\alpha \equiv dz/\mu$. Then, the radiative-transfer equation becomes:

$$-\mu \frac{dI_\nu}{d\tau_{\nu,z}} = -I_\nu + B_\nu, \quad (12)$$

which can be rewritten as:

$$-\mu \frac{d}{d\tau_{\nu,z}} \left(I_\nu e^{-\tau_{\nu,z}/\mu} \right) = B_\nu e^{-\tau_{\nu,z}/\mu}. \quad (13)$$

TRANSIT calculates the emergent intensity by integrating Equation (13) from the deep layers to the top of the atmosphere. At depth, the atmosphere is optically thick ($\tau = \tau_b \gg 1$), such that $\exp(-\tau_b/\mu) \rightarrow 0$. Therefore, the emergent intensity at the top of the atmosphere is given by:

$$I_\nu(\tau = 0, \mu) = \int_0^{\tau_b} B_\nu e^{-\tau/\mu} d\tau/\mu. \quad (14)$$

By changing variables from the angle θ to the angle on the planet hemisphere, α (related by $d \sin \theta = R_p \sin \alpha$), the emergent specific flux, Eq. (6), becomes:

$$F_\nu = \left(\frac{R_p}{d}\right)^2 \int_0^{2\pi} \int_0^{\pi/2} I_\nu \cos(\alpha) \sin(\alpha) d\alpha d\phi \quad (15)$$

$$= 2\pi \left(\frac{R_p}{d}\right)^2 \int_0^1 I_\nu \mu d\mu. \quad (16)$$

TRANSIT approximates this integral by summing over a discrete set of angles (user input), sampling from the sub-stellar point to the terminator:

$$F_\nu \approx \pi \left(\frac{R_p}{d}\right)^2 \sum_i I_\nu(\mu_i) \Delta\mu_i^2, \quad (17)$$

where the boundaries for the spans $\Delta\mu_i^2$ are calculated from the mean points between consecutive angles. By default the code adopts five angles at 0° , 20° , 40° , 60° , and 80° . We found no significant differences when varying the values or when comparing with a Gaussian quadrature procedure of a similar number of points. Finally, TRANSIT computes $I_\nu(\mu_i)$ through a Simpson numerical integration of Equation (14) and returns the emergent specific flux as measured on the surface of the planet ($d \equiv R_p$) in units of $\text{erg s}^{-1} \text{cm}^{-2} \text{cm}$:

$$F_\nu^p \approx \pi \sum_i I_\nu(\mu_i) \Delta\mu_i^2. \quad (18)$$

2.3. Atmospheric Extinction

There are multiple sources of atmospheric opacity, each one with their particular properties. The current code incorporates the main sources of opacity considered for exoplanet atmospheres: collision-induced absorption, line-transition opacities, Rayleigh scattering, and clouds.

2.3.1. Collision-induced Absorption

Collision-induced absorption is one of the main sources of atmospheric opacity. CIA occurs when particles without an intrinsic electric dipole moment collide. The collisions induce a transient dipole moment, which allows dipole transitions. The short interaction time of the collisions broadens the line profiles, generating a smooth CIA spectrum. The CIA opacity scales with the density of the colliding species, and thus becomes more relevant at the deeper, higher-pressure layers of the atmosphere (Sharp & Burrows 2007). For gas-giant planets, the two most important CIA sources are $\text{H}_2\text{-H}_2$ and, to a lesser extent, $\text{H}_2\text{-He}$ collisions. For secondary-atmosphere planets, the dominant CIA source will depend on the most abundant species in the given atmosphere. Karman et al. (2019) provides CIA data of several molecular pairs of interest for primary and secondary atmospheres.

2.3.2. Line-transition Absorption

Line transitions arise when a species absorbs or emits photons at specific wavelengths, corresponding to the characteristic energies between its electronic, rotational, and vibrational quantum levels. The atmospheric temperature and pressure affect the strength and shape of the line transitions.

TRANSIT calculates the line-transition extinction coefficient, e_ν , in a line-by-line scheme, adding the contribution from each broadened line-transition, j , as:

$$e_\nu = \sum_j S_j V(\nu - \nu_j), \quad (19)$$

where ν_j is the wavenumber of the line transition, S_j is the line strength (in cm^{-2}), and V is the line profile (Voigt). The line strength is given by:

$$S_j = \frac{\pi e^2}{m_e c^2} \frac{(gf)_j}{Z_i(T)} n_i \exp\left(-\frac{hcE_{\text{low}}^j}{k_B T}\right) \left\{1 - \exp\left(-\frac{hc\nu_j}{k_B T}\right)\right\}, \quad (20)$$

where gf_j (unitless) and E_{low}^j (in cm^{-1}) are the weighted oscillator strength and lower-state energy level of the line transition, respectively; Z_i and n_i are the partition function and number density of the isotope i , respectively; T is the atmospheric temperature; e and m_e are the electron's charge and mass, respectively; c is the speed of light, h is Planck's constant; and k_B is the Boltzmann's constant.

The Voigt profile considers the Doppler and the Michelson-Lorentz collision broadening (though, neglecting J-dependence, e.g., Barton et al. 2017). The Doppler and Lorentz half-widths at half maximum (HWHM, Goody 1995) are, respectively:

$$\sigma = \frac{\nu_j}{c} \sqrt{\frac{2k_B T \ln 2}{m_i}}, \quad (21)$$

$$\gamma = \frac{1}{c} \sum_a n_a d_a^2 \sqrt{\frac{2k_B T}{\pi} \left(\frac{1}{m_i} + \frac{1}{m_a}\right)}, \quad (22)$$

where the sub-index i refers to the absorbing species, the sub-index a of the sum runs over all species in the atmosphere. m_i and m_a are the masses of the species i and a (respectively), $d_a = r_i + r_a$ is the collision diameter between the interacting particles (with r_i and r_a the collision radii of species i and a , respectively), and n_a the number density of species a . TRANSIT computes the Voigt profiles following the algorithm of Pierluissi (1977). The wings of these line profiles are truncated at a user-defined cutoff value proportional to the Voigt HWHM of the line (typically 100–500 HWHM). We note that this is an *ad hoc* choice given the general lack of knowledge on this topic (e.g., see the discussion by Gharib-Nezhad et al. 2021).

Depending on the wavelength range and input opacity databases, a radiative-transfer calculation typically involves from thousands to billions of line transitions. Thus, the line-by-line opacity calculation is the most computationally intensive task of the process, in particular computing the Voigt profiles. Noting that the typical width of the Lorentz

HWHM, being inversely proportional to the species number density, hence to the pressure, increases several orders of magnitude from the top to the bottom of the atmosphere. The Voigt profile is then dominated by the Doppler profile at the top of the atmosphere, and by the Lorentz profile at the bottom of the atmosphere. To improve performance, we pre-compute a 3D table of Voigt profiles (see also Eqs. (2)–(11) of Harrington *et al.* 2021) with axes of wavenumber, Doppler width, and Lorentz width, covering the width ranges possible due to the pressures, temperatures, and species in the calculation. The sampling ranges and rates are user parameters, with defaults far better than needed for accuracy in current exoplanet retrievals (i.e., thousands of samples per wavenumber). Creating a high-resolution lookup table once is much quicker and more accurate than either calculating the profile per line or interpolating a lower-resolution table for each line, and, once created, accessing it takes the same time regardless of size, within reason.

The output opacity array has coarser sampling, typically 1 cm^{-1} for current exoplanet retrievals, although this value can be set by the user. When filling this array, for each line, TRANSIT selects the Voigt profile with the closest width parameters and shifts it by an integer number of profile fine samples to best match the line peak. It then samples values from the profile at the output grid’s wavenumbers.

Although, given to the nonlinearity of the radiative-transfer calculation, simply sampling from the finer Voigt profiles may bias the opacity contribution of individual lines, due to the combined contributions of the millions of lines the overall bias averages out. Rocchetto (2017) showed that for current low- and mid-resolution observations (e.g., *Spitzer* or *HST*), this approximation introduces a negligible opacity bias on model spectra at output sampling rates on the order of 1 cm^{-1} . We confirmed this during the implementation of the TRANSIT code, and also found that sampling opacity produces more accurate spectra than averaging opacity over bins. Certainly, these biases will be more severe at longer wavelengths, e.g., for *JWST*/MIRI observations. Thus, modeling such observations will require a finer sampling.

Additionally, TRANSIT incorporates a line-strength cutoff (an adjustable parameter) that prevents the computation of the weaker lines that do not significantly contribute to the opacity. Given the large span of the plausible temperatures and pressures in the atmosphere, the relative strength of different lines can change significantly from layer to layer. Therefore, TRANSIT’s cutoff threshold is relative to the largest line strength in each layer, rather than a fixed cutoff. To further minimize the number of evaluated Voigt profiles, the code automatically adds the line strengths of transitions from the same isotope that fall in a same wavenumber bin.

Lastly, TRANSIT provides the option to pre-calculate a grid of the line-by-line opacities during the initialization step. The opacity grid is a four-dimensional table that contains the opacities (in $\text{cm}^2 \text{ g}^{-1}$) evaluated over the wavenumber array, at each atmospheric pressure level, for a grid of temperatures, and for each absorbing species. The opacity grid speeds up the spectrum evaluation allowing TRANSIT to interpolate the

opacities from the table, instead of repeatedly computing the line-by-line calculations. Including the opacity grid is necessary to run an atmospheric retrieval in a reasonable amount of time (hours to days), since an MCMC typically requires on the order of millions of spectrum evaluations. These grids are computed at the wavelengths and pressures desired for a given retrieval, and thus the procedure only needs to interpolate in temperature (linear interpolation). Note that the execution time varies widely depending on the wavelength range, spectral sampling rate, number of atmospheric layers, number of spectroscopically-active species, and of course, the hardware.

2.3.3. Clouds and Rayleigh Scattering

The TRANSIT code implements Rayleigh scattering via the parametric model of Lecavelier Des Etangs *et al.* (2008), where the scattering cross section is given by $\sigma_{\text{ray}} = \sigma_0(\lambda/\lambda_0)^{-4}$, with σ_0 and λ_0 adjustable parameters. Under ideal gas law, the Rayleigh extinction coefficient is given by:

$$e_{\text{ray}} = \kappa_{\text{ray}} e_0 \frac{p}{T} \lambda^{-4}, \quad (23)$$

where κ_{ray} is a fitting parameter, and the constant $e_0 = 4.91 \times 10^{-23} \text{ K bar}^{-1} \text{ cm}^3$ is chosen such that e_{ray} matches the H_2 Rayleigh scattering of a solar-composition atmosphere when $\kappa_{\text{ray}} = 1$.

The code also implements the gray cloud-deck model that has been largely used by most atmospheric retrievals. This model is parameterized by a cloud-top pressure (p_{cloud}) below which the atmosphere becomes instantly optically thick.

2.4. Opacity Databases

The TRANSIT package handles two types of input opacity databases, cross-section (CS, opacity as a function of wavenumber and temperature) and line-by-line data (LBL, sets of individual line transition opacity parameters). Table 1 list the opacity databases currently available for TRANSIT.

Table 1. TRANSIT opacity databases

Source	Species	Type	Format
HITRAN/HITEMP ^a	H ₂ O, CO, CO ₂ , CH ₄	LBL	LT
ExoMol ^b	H ₂ O, CO, CO ₂ , CH ₄	LBL	LT
Partridge & Schwenke	H ₂ O	LBL	LT
Schwenke	TiO	LBL	LT
Plez	VO	LBL	LT
Borysow	H ₂ –H ₂ , H ₂ –He	CS	CIA
HITRAN ^c	H ₂ –H ₂ , H ₂ –He	CS	CIA

Notes. ^a HITRAN provides data for 47 additional species.

^b ExoMol provides data for 79 additional species.

^c and additional CIA pairs involving CH₄, N₂, O₂, CO₂, Ar, and air (although we note that these databases have wavelength and temperature ranges significantly more limited than those for H₂ and He).

2.4.1. Cross-section Data

Cross-section files provide tabulated opacities as a function of temperature and wavenumber. Since CIA varies smoothly

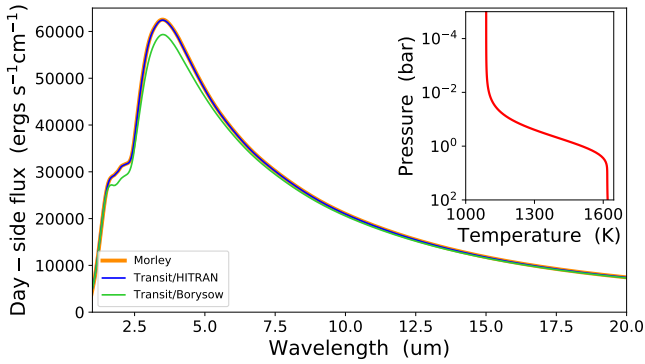


Figure 3. Model emission spectra for pure collision-induced absorption. The blue and green curves show the TRANSIT spectra for HITRAN and Borysow CIA opacities, respectively. The orange curve shows the HITRAN CIA spectrum of C. Morley. All spectra were calculated for an atmospheric model with uniform mole mixing ratios composed of 85% H_2 and 15% He, for a planet with a $1 R_{\text{Jup}}$ radius and a surface gravity of 22 m s^{-2} . The inset shows the atmospheric temperature profile as a function of pressure.

across wavenumber, this is the preferred format for CIA files. Some databases also provide line-transition data in cross-section format.

The TRANSIT input cross-section files consist of ASCII tables of the opacity normalized to the species number density (in units of $\text{cm}^{-1} \text{ amagat}^{-2}$, with $1 \text{ amagat} = n_0 = 2.68679 \times 10^{19} \text{ molecules cm}^{-3}$).

TRANSIT provides Python scripts to format the CIA data files given by the Borysow group² (Borysow et al. 2001; Borysow 2002; Borysow et al. 1988, 1989; Borysow & Frommhold 1989) and HITRAN (Richard et al. 2012; Karman et al. 2019) into its internal format.

To evaluate the CIA opacity for a given atmospheric model, TRANSIT performs a bicubic interpolation (wavenumber and temperature) from the tabulated CIA opacities (e_{cia}^t), and scales the values to units of cm^{-1} (e_{cia}), multiplying by the number density of the species:

$$e_{\text{cia}} = e_{\text{cia}}^t \frac{n_1 n_2}{n_0 n_0}, \quad (24)$$

where n_1 and n_2 are the number densities of the colliding species (in units of molecules cm^{-3}). Figure 3 shows TRANSIT emission spectra for pure H_2 – H_2 and H_2 –He CIA opacities. When compared against the models of C. Morley (priv. comm.), we agree to better than 0.5%. We also noted that the HITRAN absorption is weaker than the Borysow absorption, producing emission spectra 2%–8% stronger for this atmospheric model.

TRANSIT treats the cross-section line-transition opacity inputs in a similar manner as the CIA data files, except that the opacity is given in $\text{cm}^{-1} \text{ amagat}^{-1}$ units. TRANSIT provides a routine to re-format HITRAN and ExoMol³ cross-section data files into the format required by TRANSIT.

2.4.2. Line-by-line Data

TRANSIT stores the line-by-line opacity data into a Transition Line Information (TLI) binary file. A TLI file contains a header and the line-transition data. The header contains the number and names of databases, species, and isotopes, and the partition function per isotope as a function of temperature. The line-transition data consist of four arrays with the transition’s wavelength, lower-state energy, oscillator strength, and isotope ID. The original TRANSIT line-reading code has been rewritten in Python to make it easier for users to add functions to read additional line-list formats. Currently, the TRANSIT line reader can process line-transition files from the HITEMP/HITRAN lists (Rothman et al. 2010; Gordon et al. 2017), the H_2O list from Partridge & Schwenke (1997), the TiO list from Schwenke (1998), and the VO list from B. Plez (priv. comm.). Most line-by-line databases provide tabulated partition-function files. For the HITRAN and HITEMP databases, TRANSIT provides an implementation of the Total Internal Partition Sums code⁴ (Laraia et al. 2011). TRANSIT is also compatible with the open-source REPACK line-compression tool (Cubillos 2017), which allows it to process the ExoMol line lists (Tennyson et al. 2016). By using REPACK to identify and retain only the strongest line transitions that dominate the opacity spectrum of a given molecule, we improve the performance of the radiative-transfer calculation by discarding the large majority of weak transitions that have little impact on the outputs.

Figure 4 shows an example of the emission spectra of H_2O , CO, CO_2 , and CH_4 . A comparison with the Morley models shows a good agreement for all four cases. Figure 5 shows an example of the TiO and VO opacity spectra. The TRANSIT spectra agree well with that of Sharp & Burrows (2007). Harrington et al. (2021) present additional tests of the TRANSIT and BART codes.

3. Application to HAT-P-11b

In this section we apply our atmospheric retrieval analysis to the transit observations of the Neptune-sized planet HAT-P-11b, and compare our results to previous analyses by Fraine et al. (2014) and Chachan et al. (2019).

The exoplanet HAT-P-11b (Bakos et al. 2010) is slightly larger than Neptune in mass ($26 M_{\oplus}$) and radius ($4.7 R_{\oplus}$). The planet orbits an active K4 dwarf star ($R_s = 0.75 R_{\odot}$, $T_s = 4780 \text{ K}$), at a distance of 0.053 AU, with a period of 5 days. Given these parameters, the planetary equilibrium temperature (temperature at which the emission as blackbody balances the absorbed energy, assuming zero albedo and efficient heat redistribution) is $T_{\text{eq}} = 878 \text{ K}$.

Fraine et al. (2014) observed five transits of HAT-P-11b with the *Hubble Space Telescope*’s (HST) Wide Field Camera 3 (WFC3) G141 grism, covering the 1.1 to 1.7 μm region of the spectrum, and the *Spitzer* Infrared Array Camera (IRAC) 3.6 and 4.5 μm bands. Chachan et al. (2019) reported eight additional transits observed with HST’s STIS (G403L and G750L) and WFC3 (G102), providing a continuous wavelength coverage from 0.34 to 1.1 μm . Fraine

² astro.ku.dk/~aborysow/programs

³ <http://exomol.com/data/data-types/xsec>

⁴ http://faculty.uml.edu/robert_gamache/software/index.htm

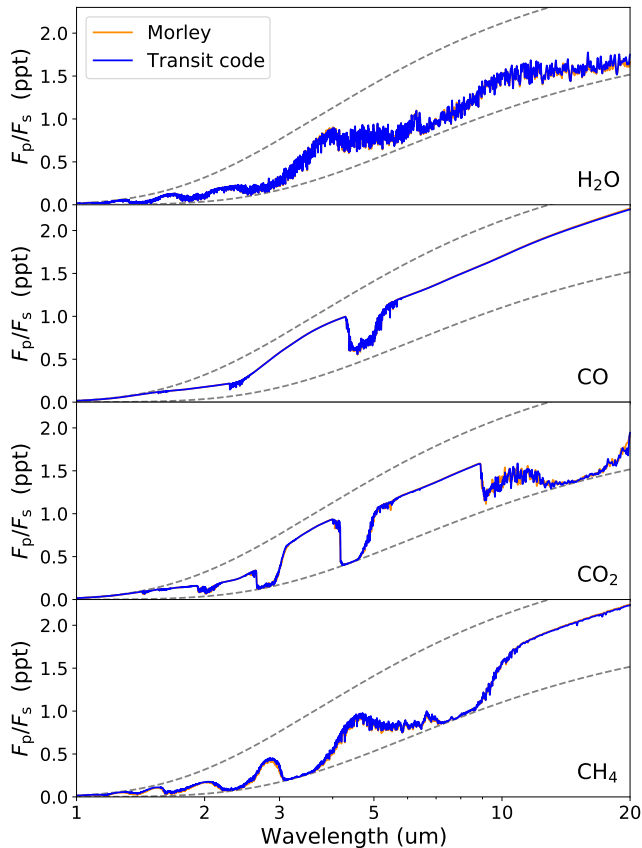


Figure 4. Model planet-to-star flux ratio spectra for water, carbon dioxide, and methane (top to bottom panels). The blue and orange solid curves show the TRANSIT-code and the Morley radiative-transfer spectra, respectively (Gaussian-smoothed for better visualization). The planetary atmospheric model is the same as in Fig. (3), with additional uniform mixing ratios of 10^{-4} for the respective species in each panel. The stellar model corresponds to a blackbody spectrum of a $1 R_{\odot}$ radius and 5700 K surface-temperature star. The dashed grey lines indicate the flux ratio for planetary blackbody spectra at 1090 and 1620 K (atmospheric maximum and minimum temperatures). The CIA opacity comes from Richard et al. (2012). For H_2O and CH_4 both models used the line lists from (Partridge & Schwenke 1997) and Yurchenko & Tennyson (2014), respectively. For CO_2 , Morley used Huang et al. (2013) and Huang et al. (2014), whereas TRANSIT used HITEMP. For CO, the Morley models used the line list from Goorvitch (1994), whereas TRANSIT used the HITEMP line list. The spectrum for each species shows a good agreement between TRANSIT and Morley’s models.

et al. (2014) and Chachan et al. (2019) presented transmission spectra binned in increasing resolving power ($R \sim 8, 15, 42, 46$) with increasing wavelength (G430L, G750L, G102, G141, respectively).

The transmission spectrum of HAT-P-11b is relatively featureless: there is no evidence for sodium ($0.59 \mu\text{m}$) nor potassium absorption ($0.77 \mu\text{m}$), and there is an evident but muted H_2O absorption feature ($1.4 \mu\text{m}$) compared to that of an atmosphere with solar-abundance composition. Noteworthy, both Fraine et al. (2014) and Chachan et al. (2019) consistently find that the *Spitzer* 3.6- and 4.5- μm transit depths are relatively shallow compared to the WFC3 transit depths. We re-analyzed the *Spitzer* light curves finding similar results (Appendix A). Fraine et al. (2014) attributed this anomaly

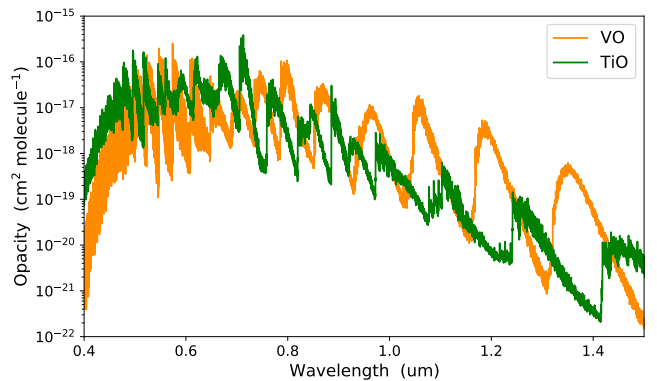


Figure 5. Near-infrared titanium- and vanadium-oxide opacity spectra. TRANSIT calculated the opacities at a temperature of 2200 K and a pressure of 10.13 bar (10 atm). Our models are consistent with Figures (4) and (5) of Sharp & Burrows (2007).

to stellar brightness variations between the different epochs, and estimated a transit depth offset of ~ 93 ppm between *HST*/G141 and *Spitzer*. However, Chachan et al. (2019) concluded from their photometric monitoring of the stellar spot coverage that such a large offset cannot be explained by stellar activity alone. In principle, given the separation in time between the *Spitzer* observations, the stellar variability should inflict a flux offset *Spitzer* observations; however, Fraine et al. (2014) found that the stellar-spot variability had a negligible impact at these wavelengths.

Fraine et al. (2014) characterized the atmospheric composition with the Self-Consistent Atmospheric Retrieval Framework for Exoplanets (SCARLET) tool (Benneke & Seager 2012, 2013) whereas Chachan et al. (2019) used the PLATON atmospheric retrieval framework (Zhang et al. 2019).

3.1. Atmospheric Retrieval

We applied our atmospheric retrieval analysis under three different scenarios. First, we retrieved on the transmission spectrum of Fraine et al. (2014), i.e., considering only the *HST*/WFC3 G141 and *Spitzer*, including a free parameter to model an offset between the *HST* and *Spitzer* transit depths. In the second and third scenarios, we modeled the transmission spectrum of Chachan et al. (2019) with and without the *Spitzer* observations. For these latter scenarios, we used the stellar-activity-corrected spectra (thus, we do not include a transit-depth offset free parameter).

We used the BART package to retrieve and constrain the atmospheric temperature, composition, gray cloud deck, and Rayleigh scattering absorption. We modeled the planetary atmosphere with a set of 101 layers, equi-spaced in log-pressure, ranging from 10^2 to 10^{-8} bar. The retrieval considers the optical and near-infrared spectrum between 0.34 and $5.5 \mu\text{m}$. Following Chachan et al. (2019), we model the atmospheric temperature as an isothermal profile. Unlike both Fraine et al. (2014) and Chachan et al. (2019), we did not assume abundances in thermochemical equilibrium, since this is highly unlikely at the temperatures expected for HAT-P-11b, as disequilibrium processes start to take place at

Table 2. BART Atmospheric Retrievals of HAT-P-11b

Parameter	Analyzed dataset:	Fraine et al. (2014)	Chachan et al. (2019)	Chachan et al. (2019)
	Prior	<i>HST</i> /G141 + <i>Spitzer</i> ^a	<i>HST</i> ^a	<i>HST</i> + <i>Spitzer</i> ^a
T_0 (K)	Uniform (200, 3000)	860^{+420}_{-330}	1120^{+245}_{-210}	1120^{+180}_{-140}
$R_p(R_\oplus)$ at $p_0 = 0.1$ bar	Uniform (2.0, 7.0)	$4.19^{+0.08}_{-0.19}$	$4.12^{+0.17}_{-0.13}$	$4.05^{+0.09}_{-0.09}$
$\log_{10}(p_{\text{cloud}}/\text{bar})$	Uniform (-6, 2)	$-1.9^{+2.4}_{-1.9}$	$-2.8^{+1.8}_{-0.9}$	$-3.6^{+0.9}_{-0.5}$
$\log_{10}(\kappa_{\text{ray}})$	Uniform (-5, 5)	...	$-1.2^{+2.4}_{-2.5}$	$-0.7^{+2.6}_{-3.0}$
<i>HST</i> - <i>Spitzer</i> offset (ppm)	Uniform (-200, 200)	102^{+34}_{-27}
$\log_{10}(\text{H}_2\text{O})$	Uniform (-10, 0)	$-1.5^{+0.8}_{-1.5}$	$-2.9^{+1.3}_{-1.7}$	$-1.7^{+0.8}_{-1.0}$
$\log_{10}(\text{CH}_4)$	Uniform (-10, 0)	$-6.7^{+2.3}_{-2.2}$	$-2.6^{+1.4}_{-1.7}$	$-7.5^{+1.8}_{-1.7}$
$\log_{10}(\text{CO})$	Uniform (-10, 0)	$-5.4^{+3.1}_{-3.1}$	$-5.6^{+3.1}_{-3.0}$	$-6.4^{+2.7}_{-2.5}$
$\log_{10}(\text{CO}_2)$	Uniform (-10, 0)	$-6.7^{+2.6}_{-2.2}$	$-5.3^{+2.7}_{-3.2}$	$-7.8^{+1.8}_{-1.5}$

Notes. ^a Reported values correspond to the marginal posterior distribution's median and boundaries of the 68% central credible interval (Andrae 2010).

$T \lesssim 2000$ K (Moses 2014). We thus modeled the composition as constant-with-altitude volume-mixing-ratios profiles for H_2O , CH_4 , CO , and CO_2 (the main species expected to dominate the observed transmission spectrum). While the constant-with-altitude assumption is likely unphysical, from a statistical standpoint, the limited precision and spectral coverage of current observations does not allow to constrain more complex models. Thus, the adoption of such simplistic retrieval approximations should be considered as first-order estimations. Certainly, the next generation of telescopes will require a more accurate description of the planetary physical properties (e.g., Rocchetto et al. 2016; Blecic et al. 2017; Caldas et al. 2019). The code assumes that the planet has a primary atmosphere, where the remaining bulk of the composition is assumed to be H_2 and He at a solar-composition ratio (Asplund et al. 2009), such that the total mixing ratio is 1.0. We neglect the contribution by Na and K, since the data does not indicate that they are detectable. We used the HITEMP opacities for CH_4 (Hargreaves et al. 2020), CO (Li et al. 2015), and CO_2 (Rothman et al. 2010). For H_2O we used the ExoMol opacities (Polyansky et al. 2018) processed with the REPACK line compression tool (Cubillos 2017). The model also included CIA opacities for $\text{H}_2\text{-H}_2$ and $\text{H}_2\text{-He}$ (Karman et al. 2019). For the calculation of the line-by-line opacities, we set a cutoff at 10^{-10} times the strongest lines. This threshold cutoff can introduce transit-depth biases on the order of $\lesssim 10^{-1}$ ppm (far lower than the typical observing uncertainty), while significantly speeding up the calculations. We also considered a gray cloud deck in the atmospheric model parameterized by the cloud-deck top pressure p_{cloud} . For the retrievals of the Chachan et al. (2019) spectrum we also included the parametric Rayleigh-scattering model described in Section 2.3.3.

BART calculates the altitude (the radius) of each layer using the hydrostatic-equilibrium equation:

$$\frac{dp}{dz} = -\rho g = -\rho(z) \frac{GM_p}{z^2}, \quad (25)$$

where z and ρ are the altitude and mass density of each layer, respectively, and $g(z) = GM_p/z^2$ is the gravity, with G the gravitational constant and M_p the mass of the planet. A retrieval free parameter sets the reference planetary radius R_p at a fiducial pressure level of 0.1 bar.

One of the main differences in the modeling approach between Fraine et al. (2014) and Chachan et al. (2019) is how they combine data from non-simultaneous observations. While Fraine et al. (2014) includes a free parameter that offsets the WFC3 and *Spitzer* data points, Chachan et al. (2019) apply a wavelength-dependent stellar-activity correction leading to shallower transit depths at short wavelengths and larger transit depths at longer wavelengths. In this study, we aimed at reproducing the main analyses of Fraine et al. (2014) and Chachan et al. (2019), and thus we adopted these same assumptions. Table 2 summarizes the retrieval free parameters and their priors for each of the three scenarios.

3.1.1. Fraine et al. (2014) Retrieval Results

Figure 6 and Table 2 show the best-fitting spectrum and posterior distributions for the BART atmospheric retrieval on the Fraine et al. (2014) data set. Our best-fitting model yields $\chi^2_{\text{red}} = 1.05$, indicating a good fit. Although the comparison is not direct, we found results that are qualitatively similar to those of Fraine et al. (2014). We found an offset between *HST* and *Spitzer* with a median of 103^{+34}_{-28} ppm, consistent with the 93 ppm value reported by Fraine et al. (2014). The pairwise posterior distributions show little correlation between the offset and the other parameters; however, as discussed by Yip et al. (2021), such treatments are often *ad hoc* corrections, and the results should be taken with care. The $\log(\text{H}_2\text{O})$ - $\log(p_{\text{cloud}})$ pairwise panel shows two solution modes: the atmosphere can either have a high super-solar H_2O abundance independent of the cloud coverage or an anti-correlated H_2O - p_{cloud} mode. This is qualitatively consistent with the posterior distribution shown in Fig. 3 of Fraine et al. (2014). Our H_2O marginal posterior peaks at $\sim 250\times$ solar metallicity (the solar abundance of H_2O in ther-

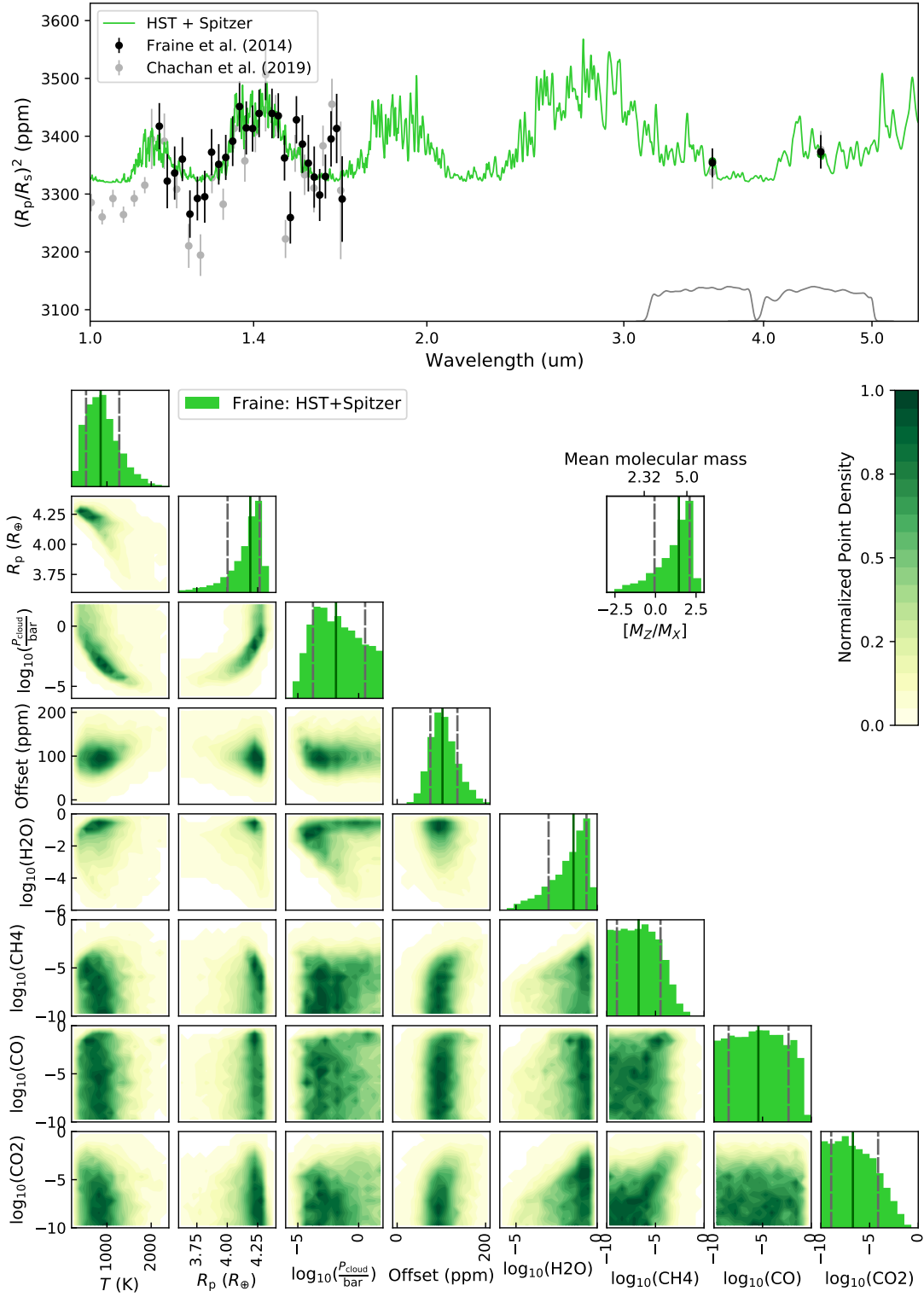


Figure 6. **Top:** HAT-P-11b transmission spectra. The black points with error bars denote the *HST* WFC3/G141 and *Spitzer* IRAC data and their 1σ uncertainties reported by Fraine et al. (2014). The gray points with error bars denote the data reported by Chachan et al. (2019). The green curve shows the BART best-fitting spectrum to the Fraine et al. (2014) dataset. The *HST* points were adjusted downwards according to the retrieved offset. The gray curves at the bottom show the *Spitzer* transmission filters. **Bottom:** Pairwise and marginal posterior probability distribution to the Fraine et al. (2014) dataset. The solid and dashed vertical lines denote the posterior’s median and boundaries of the 68% credible interval, respectively (Table 2).

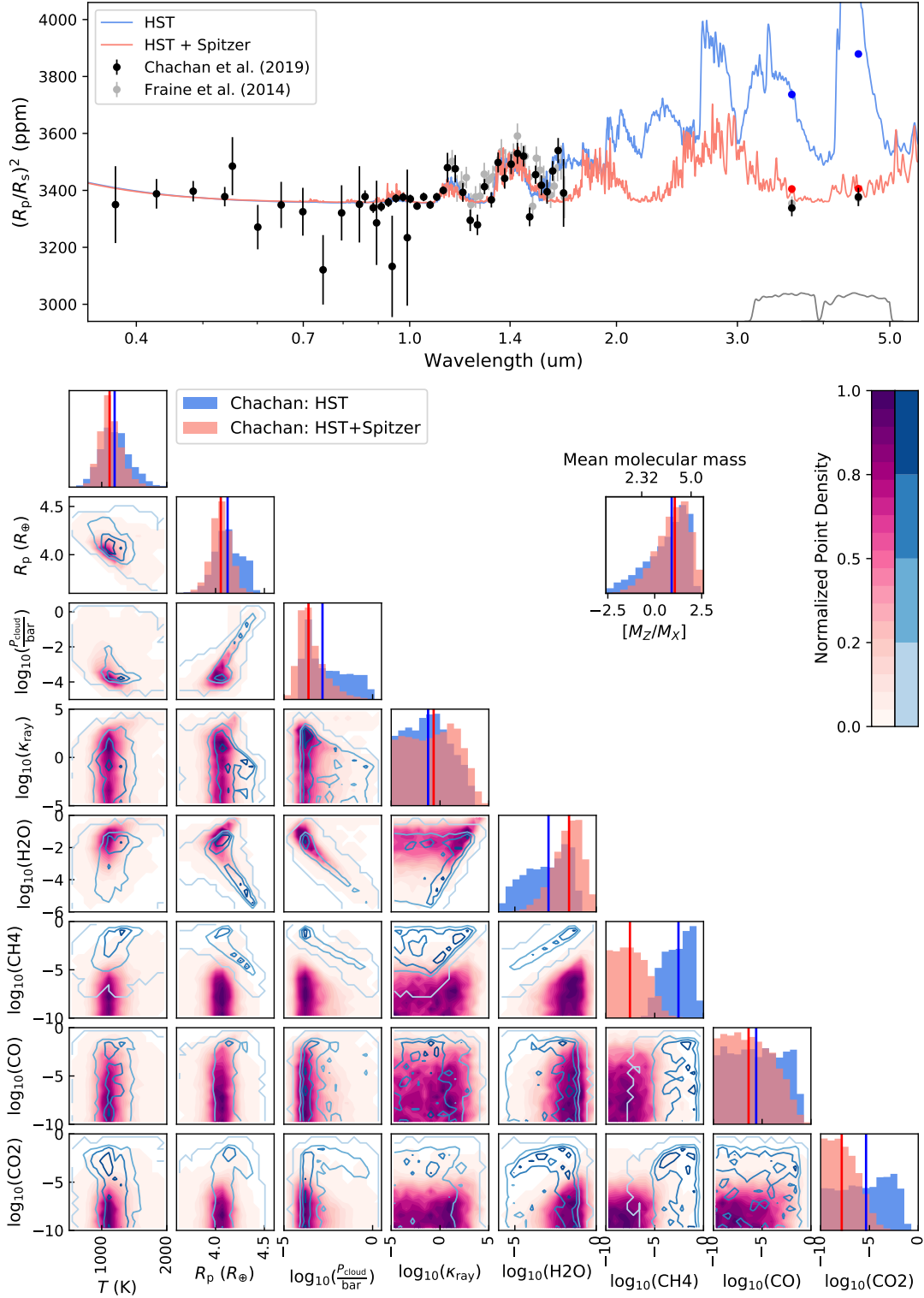


Figure 7. Top: HAT-P-11b transmission spectra. The black points with error bars denote the *HST* and *Spitzer* IRAC data and their 1σ uncertainties reported by Chachan et al. (2019). The gray points with error bars denote the data reported by Fraine et al. (2014). The pink and blue curves show the BART best-fitting spectrum to the Chachan et al. (2019) datasets (with and without considering the *Spitzer* observations, respectively). The gray curves at the bottom show the *Spitzer* transmission filters. **Bottom:** Pairwise and marginal posterior probability distribution to the Chachan et al. (2019) dataset (the pink shaded areas show the retrieval posteriors of the *HST* and *Spitzer* data, whereas the blue contours show that of the *HST* data alone). The red and blue solid vertical lines denote the posterior’s median for the retrieval with and without considering the *Spitzer* observations, respectively. We omitted plotting the credible interval boundaries to avoid cluttering (their values are available in Table 2).

mochemical equilibrium at 900 K is $\sim 10^{-3}$). The posterior distribution of the cloud-top pressure is broad, constrained to values $p_{\text{cloud}} \gtrsim 20$ mbar. Both results are consistent with those of Fraine *et al.* (2014), who found a best-fit metallicity of $190\times$ solar and constrained the cloud deck to pressures higher than 10 mbar. From our posterior we derived a super-solar metals mass fraction of $[M_Z/M_X] = 1.4^{+0.7}_{-1.5}$, with the caveat that we estimated this value from the molecular abundances (largely dominated by H_2O), whereas Fraine *et al.* (2014) directly fit for the metallicity.

The key to constrain the enhanced atmospheric abundance is the amplitude of the $1\text{--}2\ \mu\text{m}$ absorption feature. A higher abundance of heavy elements implies a higher mean molecular mass, hence a smaller scale height, and a smaller feature amplitude. The high H_2O abundance, thus, allows the model to match the observed H_2O -band amplitude between 1 and $2\ \mu\text{m}$. The cloudy solution results from the combination of the cloud deck, H_2O abundance, and hydrostatic-equilibrium solution. As the H_2O abundance increases, the amplitude of the $1.4\ \mu\text{m}$ feature becomes more prominent. The presence of the gray cloud deck mutes the amplitude of the feature to maintain the match to the observed amplitude (hence the anti-correlation between p_{cloud} and H_2O abundance). At the same time, the T and R_p at 0.1 bar must also vary to preserve the absolute value of the transit depth at the observed values (see the correlation in the pairwise posteriors in Fig. 6).

The abundances of CO, CO_2 , and CH_4 remained largely unconstrained, showing nearly flat posterior histograms, finding at most upper limits. This is an expected outcome, since the H_2O opacity dominates the entire spectral range probed by these observations, whereas the CO and CO_2 abundance hinge predominantly on the *Spitzer* $4.5\ \mu\text{m}$ observation and the CH_4 abundance hinges predominantly on the *Spitzer* $3.6\ \mu\text{m}$ observation. Combined with the larger number and better spectral resolution of the *HST* observations, the given low-resolution data can better constrain the H_2O features at the shorter wavelengths, whereas CO, CO_2 , and CH_4 can only be constrained if their spectroscopic signatures raise above the level set by the H_2O absorption at the longer wavelengths.

We observed no artifacts in the posterior sampling due to the discrete nature of the atmospheric profile model. This is a particularly relevant concern when including cloud models that make the atmosphere instantly opaque below a certain pressure level, because the resulting cloud deck location gets discretized by the atmospheric pressure sampling. In this case, it is likely that the posterior distributions constrained by these datasets are broad enough such that effect of the discrete sampling are not seen (e.g., over 1 dex for p_{cloud}). Cubillos & Blečić (2021) show a better implementation of a cloud-deck model by interpolating the atmospheric sampling model at the pressure location of the opaque cloud deck.

3.1.2. Chachan *et al.* (2019) Retrieval Results

Figure 7 and Table 2 show the best-fitting spectra and posterior distributions for the BART atmospheric retrievals on the Chachan *et al.* (2019) data sets. We found reasonably

good fits to the *HST* observations; however, no model were able to fit simultaneously the transit depths of the *HST* and *Spitzer* observations. Given the *HST* observations, all models predict larger transit depth at the *Spitzer* bands. Consequently, our best-fitting χ^2_{red} values increased from 1.5 to 2.3 when we include the *Spitzer* data in the retrieval. Chachan *et al.* (2019) found similar results, with χ^2_{red} increasing from 1.9 to 2.8. Since the retrievals of Chachan *et al.* (2019) included a free parameter scaling the instrumental errors (σ_{mult}), they naturally obtained a larger σ_{mult} when including the *Spitzer* observations, and thus found broader posterior distributions. In contrast, we generally found narrower posterior distributions when including the *Spitzer* observations. As expected, when the retrieval did not consider the *Spitzer* observations, the CO and CO_2 abundances are completely unconstrained (the dominant absorption feature of these molecules is in the $4.5\ \mu\text{m}$ band). Including the shallow *Spitzer* transit depths places more stringent constraints on the CO and CO_2 abundance upper limits.

The CH_4 abundance posterior is an interesting case, the Chachan *et al.* (2019) *HST* transmission spectrum shows an increase with wavelength at the red-end tail ($\sim 1.6\ \mu\text{m}$) that coincides with a CH_4 band. Thus, the *HST* data alone suggest a high CH_4 abundance ($\log(\text{CH}_4) = -2.6^{+1.4}_{-1.7}$), which is discouraged by the inclusion of the shallow $3.6\ \mu\text{m}$ observation ($\log(\text{CH}_4) = -7.5^{+1.8}_{-1.7}$). In fact, the retrieval on the *HST* data alone places a tight correlation between the H_2O and CH_4 abundances (with CH_4 slightly more abundant) that extends over several orders of magnitude. Including the *Spitzer* data breaks the H_2O – CH_4 correlation, allowing the H_2O abundance to adopt higher values (in a similar fashion to the run without CH_4 of Chachan *et al.* 2019).

Overall, we found similar behavior for the retrieved haze and cloud parameters as Chachan *et al.* (2019). The cloud-top pressures adopted lower values when including the *Spitzer* observations, though we obtained p_{cloud} values ~ 1.5 dex lower than those of Chachan *et al.* (2019). The Rayleigh scattering scale factor remained largely unconstrained for both scenarios, with upper limits ~ 1 dex larger than the expected values for H_2 Rayleigh scattering.

We derived super-solar metals mass fraction (on the order of $10\times$ solar) for both the *HST*-only retrieval ($[M_Z/M_X] = 0.9^{+0.8}_{-1.5}$) and the retrieval including the *Spitzer* observations ($[M_Z/M_X] = 1.1^{+0.8}_{-1.0}$). In contrast, Chachan *et al.* (2019) found $10\times$ sub-solar and $100\times$ super-solar metallicities, respectively.

We do not have a clear explanation for this discrepancy. We can only speculate that this occurs because of the difference between thermochemical-equilibrium chemistry (Chachan *et al.* 2019) and free constant-with-altitude chemistry (this work), which is arguably the main difference between these two analyses. An *a posteriori* equilibrium-chemistry calculation according to our best-fit results ($T = 1120$ K and $1.1\times$ solar metallicity) shows CO/ H_2O ratios near unity, inconsistent with our posterior distributions, which show lower relative CO abundances. It is likely that the set of high-metallicity solutions found here

are not allowed under chemical equilibrium (at least under the assumption of solar elemental ratios), thus leading to different posterior distributions. We note also that equilibrium chemistry often leads to non constant-with-altitude abundance profiles, particularly for non-isothermal temperature profiles, which makes the discrepancy between our results and those of Chachan et al. (2019) less simple to interpret. Finally, we note that the correlations between parameters are strongly enhanced when we neglect the *Spitzer* observations (Fig. 7).

4. Conclusions

In this article we presented the open-source, open-development TRANSIT code to compute exoplanet spectra. TRANSIT is a core package of the BART project to characterize exoplanet atmospheres in a statistically robust manner. BART is jointly presented here, in Harrington et al. (2021), and in Blečić et al. (2021). The TRANSIT package solves the one-dimensional radiative-transfer equation to calculate transmission or emission spectra. The current version of the code accounts for opacities from molecular line-transition, collision-induced absorption, gray cloud decks, and Rayleigh scattering. We compared the TRANSIT emission spectra against models of C. Morley, finding a good agreement. TRANSIT also accurately reproduced the opacity spectra of Sharp & Burrows (2007). The project's source code and documentation are available at <https://github.com/exosports/transit>.

We further applied the BART atmospheric retrieval analysis to the *HST* and *Spitzer* transit observations of HAT-P-11b (Fraine et al. 2014; Chachan et al. 2019) assuming an isothermal temperature profile, constant-with-altitude composition of H₂O, CO, CO₂, and CH₄ (i.e., without assuming equilibrium chemistry), gray clouds, and Rayleigh scattering. The transmission spectra constrains mainly the H₂O abundance through its 1.4 μm band. When retrieving on the transmission spectra of Fraine et al. (2014) alone (*HST*/WFC3/G141 and *Spitzer*) we found a ~10–100× super-solar enhancement of metals, determined by the retrieved high H₂O abundance. Alternatively, models with high-altitude cloud decks fit the observations well. Other species abundances (CH₄, CO, and CO₂) remained largely unconstrained.

Given the significant stellar activity of HAT-P-11, it is likely that the *HST* and *Spitzer* transit depths have an offset due to the unknown absolute calibration of the system flux. These retrievals made use of a free parameter to account for this offset; however, this extra degree of freedom can mask spectral features, limiting our capacity to find atmospheric constraints. These results are consistent with the atmospheric retrieval analysis of Fraine et al. (2014).

When retrieving on the transmission spectra of Chachan et al. (2019), our result do not totally agree with the previous work. Chachan et al. (2019) concluded that their atmospheric analysis is primarily driven by the *HST* observations. However, when taking the transmission data at face value, the *Spitzer* observations change the outputs significantly. Neither their nor our models were able to fit well all observations simultaneously. By including the *Spitzer* observations,

the Chachan et al. (2019) retrievals favored metallicities three orders of magnitude larger. In our case, the shallow *Spitzer* 3.6 μm transit depth (relative to the *HST* transit depth) ruled out the presence of CH₄ in the atmosphere, in contrast to the CH₄ abundances higher than H₂O for the retrieval without the *Spitzer* observations. Though, for both of our retrieval of the Chachan et al. (2019) transmission spectra (with and without the *Spitzer* observations) we found super-solar metals mass fractions (~10× solar values). Our results agree better than Chachan et al. (2019) with the extrapolation of the solar-system mass-metallicity relationship (Kreidberg et al. 2014), though we remark that we are estimating metals mass fractions rather than metallicities. We suspect that the different conclusions between our work and those of Chachan et al. (2019) arises from the different choice to model the chemistry (free constant-with-altitude vs. thermochemical equilibrium).

The case of HAT-P-11b highlights that exoplanet atmospheric retrievals rely on multiple factors, where the adopted modeling assumptions about the physics or statistics impact the outcome as significantly as the observations themselves. Given the little prior knowledge we have about any given system, many of these assumptions do not have strong grounds; they are guesses. Whether an atmosphere is under thermochemical equilibrium or not leads to widely different compositions, and this possibly explains the difference in the estimated metallicity between our analysis and Chachan et al. (2019). Whether we trust stitching of non-simultaneous observations or we apply an uncertainty correction leads one to favor one (sub)set of observations over another, reaching different conclusions. Thus, contrasting multiple analyses of a given observation can help us to attain a better understanding not only about planetary physics but also about the atmospheric retrieval approach. The tools we have presented here prepare us to better study the diversity of exoplanet atmospheres that will be observed in the future. Hopefully, laboratory advancements and the development of next-generation telescopes, like the *JWST* will enable the study of exoplanets with unprecedented detail.

A compendium of the BART analyses published in this work is available in a Zenodo repository located at <https://doi.org/10.5281/zenodo.5602872>.

We thank C. Morley and J. Fortney for useful conversations and for providing radiative-transfer spectra for comparison. We thank the anonymous referees for their time and valuable comments. We thank contributors to the Python Programming Language and the free and open-source community (see Software Section below). We drafted this article using the aastex6.2 latex template (AAS Journals Team & Hendrickson 2018), with some further style modifications that are available at <https://github.com/pcubillos/ApJtemplate>. P.C. was supported by the Fulbright Program for Foreign Students. J.B. was supported by the NASA Earth and Space Science Fellowship, grant NNX12AL83H and the NASA Exoplanets Research Program, grant NNX17AC03G. This

work was supported by the Science Mission Directorate’s Planetary Atmospheres Program, grant NNX12AI69G, the NASA Astrophysics Data Analysis Program grant NNX13AF38G, and the NASA Exoplanets Research Program, grant NNX17AB62G. P.R. acknowledges support from CONICYT project Basal AFB-170002. Part of this work is based on observations made with the *Spitzer Space Telescope*, which is operated by the Jet Propulsion Laboratory, California Institute of Technology under a contract with NASA. Part of this work is based on observations made with the NASA/ESA Hubble Space Telescope, obtained from the data archive at the Space Telescope Science Institute. This research has made use of NASA’s Astrophysics Data System Bibliographic Services.

Software: BART (<https://github.com/exosports/BART>), MC3 (Cubillos *et al.* 2017), TEA (Blecic *et al.* 2016), REPACK (Cubillos 2017), NUMPY (Harris *et al.* 2020), SCIPY (Virtanen *et al.* 2020), SYMPY (Meurer *et al.* 2017), MATPLOTLIB (Hunter 2007), IPYTHON (Pérez & Granger 2007), AASTeX6.2 (AAS Journals Team & Hendrickson 2018), ApJtemplate (<https://github.com/pcubillos/ApJtemplate>), and BIBMANAGER⁵ (Cubillos 2019).

References

- AAS Journals Team, & Hendrickson, A. 2018, Aasjournals/Aastex60: Version 6.2 Official Release, *ADS*
- Andrae, R. 2010, arXiv e-prints, arXiv:1009.2755, *ADS*, 1009.2755
- Andrews, D. G. 2000, An Introduction to Atmospheric Physics, *ADS*
- Asplund, M., Grevesse, N., Sauval, A. J., & Scott, P. 2009, *ARA&A*, 47, 481, *ADS*, 0909.0948
- Bakos, G. Á. *et al.* 2010, *ApJ*, 710, 1724, *ADS*, 0901.0282
- Barstow, J. K., Aigrain, S., Irwin, P. G. J., & Sing, D. K. 2017, *ApJ*, 834, 50, *ADS*, 1610.01841
- Barton, E. J., Hill, C., Yurchenko, S. N., Tennyson, J., Dudaryonok, A. S., & Lavrentieva, N. N. 2017, *JQSRT*, 187, 453, *ADS*, 1610.09008
- Benneke, B., & Seager, S. 2012, *ApJ*, 753, 100, *ADS*, 1203.4018
- Benneke, B., & Seager, S. 2013, *ApJ*, 778, 153, *ADS*, 1306.6325
- Blecic, J., Dobbs-Dixon, I., & Greene, T. 2017, *ApJ*, 848, 127, *ADS*, 1803.06678
- Blecic, J., Harrington, J., & Bowman, M. O. 2016, *ApJS*, 225, 4, *ADS*, 1505.06392
- Blecic, J. *et al.* 2021, arXiv e-prints, arXiv:2104.12525, *ADS*, 2104.12525
- Borysow, A. 2002, *A&A*, 390, 779, *ADS*
- Borysow, A., & Frommhold, L. 1989, *ApJ*, 341, 549, *ADS*
- Borysow, A., Frommhold, L., & Moraldi, M. 1989, *ApJ*, 336, 495, *ADS*
- Borysow, A., Jorgensen, U. G., & Fu, Y. 2001, *JQSRT*, 68, 235, *ADS*
- Borysow, J., Frommhold, L., & Birnbaum, G. 1988, *ApJ*, 326, 509, *ADS*
- Burrows, A., Hubeny, I., & Sudarsky, D. 2005, *ApJL*, 625, L135, *ADS*, astro-ph/0503522
- Burrows, A. *et al.* 1997, *ApJ*, 491, 856, *ADS*, astro-ph/9705201
- Caldas, A., Leconte, J., Selsis, F., Waldmann, I. P., Bordé, P., Rocchetto, M., & Charnay, B. 2019, *A&A*, 623, A161, *ADS*, 1901.09932
- Campo, C. J. *et al.* 2011, *ApJ*, 727, 125, *ADS*, 1003.2763
- Chachan, Y. *et al.* 2019, *AJ*, 158, 244, *ADS*, 1910.07523
- Charbonneau, D. *et al.* 2005, *ApJ*, 626, 523, *ADS*, astro-ph/0503457
- Cubillos, P., Harrington, J., Loredó, T. J., Lust, N. B., Blecic, J., & Stemm, M. 2017, *AJ*, 153, 3, *ADS*, 1610.01336
- Cubillos, P., Harrington, J., Madhusudhan, N., Foster, A. S. D., Lust, N. B., Hardy, R. A., & Bowman, M. O. 2014, *ApJ*, 797, 42, *ADS*, 1411.3093
- Cubillos, P. *et al.* 2013, *ApJ*, 768, 42, *ADS*, 1303.5468
- Cubillos, P. E. 2017, *ApJ*, 850, 32, *ADS*, 1710.02556
- Cubillos, P. E. 2019, bibmanager: A BibTeX manager for LaTeX projects, Zenodo, doi:10.5281/zenodo.2547042, *ADS*
- Cubillos, P. E., & Blecic, J. 2021, *MNRAS*, 505, 2675, *ADS*, 2105.05598
- Drummond, B., Carter, A. L., Hébrard, E., Mayne, N. J., Sing, D. K., Evans, T. M., & Goyal, J. 2019, *MNRAS*, 486, 1123, *ADS*, 1903.10997
- Dudhia, A. 2017, *JQSRT*, 186, 243, *ADS*
- Evans, T. M. *et al.* 2017, *Nature*, 548, 58, *ADS*, 1708.01076
- Fortney, J. J. 2005, *MNRAS*, 364, 649, *ADS*, astro-ph/0509292
- Fortney, J. J. *et al.* 2016, arXiv e-prints, arXiv:1602.06305, *ADS*, 1602.06305
- Fortney, J. J., Shabram, M., Showman, A. P., Lian, Y., Freedman, R. S., Marley, M. S., & Lewis, N. K. 2010, *ApJ*, 709, 1396, *ADS*, 0912.2350
- Fraine, J. *et al.* 2014, *Nature*, 513, 526, *ADS*, 1409.8349
- Gandhi, S., & Madhusudhan, N. 2018, *MNRAS*, 474, 271, *ADS*, 1710.06433
- Gardner, J. P. *et al.* 2006, *SSRv*, 123, 485, *ADS*, astro-ph/0606175
- Gharib-Nezhad, E., Iyer, A. R., Line, M. R., Freedman, R. S., Marley, M. S., & Batalha, N. E. 2021, *ApJS*, 254, 34, *ADS*, 2104.00264
- Goody, R. 1995, Principles of Atmospheric Physics and Chemistry, *ADS*
- Goorvitch, D. 1994, *ApJS*, 95, 535, *ADS*
- Gordon, I. E. *et al.* 2017, *JQSRT*, 203, 3, *ADS*
- Hansen, C. J., Schwartz, J. C., & Cowan, N. B. 2014, *MNRAS*, 444, 3632, *ADS*, 1402.6699
- Hargreaves, R. J., Gordon, I. E., Rey, M., Nikitin, A. V., Tyuterev, V. G., Kochanov, R. V., & Rothman, L. S. 2020, *ApJS*, 247, 55, *ADS*, 2001.05037
- Harrington, J. *et al.* 2021, arXiv e-prints, arXiv:2104.12522, *ADS*, 2104.12522
- Harris, C. R. *et al.* 2020, *Nature*, 585, 357, *ADS*, 2006.10256
- Huang, X., Freedman, R. S., Tashkun, S. A., Schwenke, D. W., & Lee, T. J. 2013, *JQSRT*, 130, 134, *ADS*
- Huang, X., Gamache, R. R., Freedman, R. S., Schwenke, D. W., & Lee, T. J. 2014, *JQSRT*, 147, 134, *ADS*
- Hunter, J. D. 2007, *Computing In Science & Engineering*, 9, 90
- Karman, T. *et al.* 2019, *Icarus*, 328, 160, *ADS*
- Kempton, E. M. R., Lupu, R., Owusu-Asare, A., Slough, P., & Cale, B. 2017, *PASP*, 129, 044402, *ADS*, 1611.03871
- Kreidberg, L. *et al.* 2014, *ApJL*, 793, L27, *ADS*, 1410.2255
- Laraia, A. L., Gamache, R. R., Lamouroux, J., Gordon, I. E., & Rothman, L. S. 2011, *Icarus*, 215, 391, *ADS*
- Lavie, B. *et al.* 2017, *AJ*, 154, 91, *ADS*, 1610.03216
- Lecavelier Des Etangs, A., Pont, F., Vidal-Madjar, A., & Sing, D. 2008, *A&A*, 481, L83, *ADS*, 0802.3228
- Li, G., Gordon, I. E., Rothman, L. S., Tan, Y., Hu, S.-M., Kassi, S., Campargue, A., & Medvedev, E. S. 2015, *ApJS*, 216, 15, *ADS*
- Line, M. R. *et al.* 2013, *ApJ*, 775, 137, *ADS*, 1304.5561
- Lothringer, J. D., & Barman, T. S. 2020, *AJ*, 159, 289, *ADS*, 2005.03056
- Lupu, R. E., Marley, M. S., Lewis, N., Line, M., Traub, W. A., & Zahnle, K. 2016, *AJ*, 152, 217, *ADS*, 1604.05370
- MacDonald, R. J., & Madhusudhan, N. 2017, *MNRAS*, 469, 1979, *ADS*, 1701.01113
- Madhusudhan, N., Agúndez, M., Moses, J. I., & Hu, Y. 2016, *SSRv*, 205, 285, *ADS*, 1604.06092
- Madhusudhan, N., & Seager, S. 2010, *ApJ*, 725, 261, *ADS*, 1010.4585
- Malik, M. *et al.* 2017, *AJ*, 153, 56, *ADS*, 1606.05474
- Mandel, K., & Agol, E. 2002, *ApJL*, 580, L171, *ADS*, astro-ph/0210099
- Marley, M. S., Ackerman, A. S., Cuzzi, J. N., & Kitzmann, D. 2013, Clouds and Hazes in Exoplanet Atmospheres, ed. S. J. Mackwell, A. A. Simon-Miller, J. W. Harder, & M. A. Bullock, 367, *ADS*

⁵ <https://bibmanager.readthedocs.io>

- Marley, M. S., Saumon, D., Guillot, T., Freedman, R. S., Hubbard, W. B., Burrows, A., & Lunine, J. I. 1996, *Science*, 272, 1919, [ADS](#), [astro-ph/9606036](#)
- Mayne, N. J. et al. 2014, *A&A*, 561, A1, [ADS](#)
- McKay, C. P., Pollack, J. B., & Courtin, R. 1989, *Icarus*, 80, 23, [ADS](#)
- Meurer, A. et al. 2017, *PeerJ Computer Science*, 3, e103
- Min, M., Ormel, C. W., Chubb, K., Helling, C., & Kawashima, Y. 2020, *A&A*, 642, A28, [ADS](#), [2006.12821](#)
- Mollière, P., Wardenier, J. P., van Boekel, R., Henning, T., Molaverdikhani, K., & Snellen, I. A. G. 2019, *A&A*, 627, A67, [ADS](#), [1904.11504](#)
- Morley, C. V., Fortney, J. J., Marley, M. S., Zahnle, K., Line, M., Kempton, E., Lewis, N., & Cahoy, K. 2015, *ApJ*, 815, 110, [ADS](#), [1511.01492](#)
- Moses, J. I. 2014, *Philosophical Transactions of the Royal Society of London Series A*, 372, 20130073, [ADS](#), [1307.5450](#)
- Moses, J. I. et al. 2013, *ApJ*, 777, 34, [ADS](#), [1306.5178](#)
- Nymeyer, S. et al. 2011, *ApJ*, 742, 35, [ADS](#), [1005.1017](#)
- Öberg, K. I., Murray-Clay, R., & Bergin, E. A. 2011, *ApJL*, 743, L16, [ADS](#), [1110.5567](#)
- Oppenheimer, B. R., Kulkarni, S. R., Matthews, K., & van Kerkwijk, M. H. 1998, *ApJ*, 502, 932, [ADS](#), [astro-ph/9802299](#)
- Partridge, H., & Schwenke, D. W. 1997, *JChPh*, 106, 4618, [ADS](#)
- Pérez, F., & Granger, B. E. 2007, *Computing in Science and Engineering*, 9, 21
- Pierluissi, J. 1977, *JQSRT*, 18, 555, [ADS](#)
- Polyansky, O. L., Kyuberis, A. A., Zobov, N. F., Tennyson, J., Yurchenko, S. N., & Lodi, L. 2018, *MNRAS*, 480, 2597, [ADS](#), [1807.04529](#)
- Rackham, B. V., Apai, D., & Giampapa, M. S. 2018, *ApJ*, 853, 122, [ADS](#), [1711.05691](#)
- Richard, C. et al. 2012, *JQSRT*, 113, 1276, [ADS](#)
- Rocchetto, M. 2017, PhD thesis, University College London
- Rocchetto, M., Waldmann, I. P., Venot, O., Lagage, P. O., & Tinetti, G. 2016, *ApJ*, 833, 120, [ADS](#), [1610.02848](#)
- Rojo, P. M. 2006, PhD thesis, Cornell University
- Rothman, L. S. et al. 2010, *JQSRT*, 111, 2139, [ADS](#)
- Rybicki, G. B., & Lightman, A. P. 1986, *Radiative Processes in Astrophysics*, [ADS](#)
- Schwartz, J. C., & Cowan, N. B. 2017, *PASP*, 129, 014001, [ADS](#), [1607.01013](#)
- Schwenke, D. W. 1998, *Faraday Discussions*, 109, 321, [ADS](#)
- Seager, S. 2010, *Exoplanet Atmospheres: Physical Processes*, [ADS](#)
- Seager, S., Richardson, L. J., Hansen, B. M. S., Menou, K., Cho, J. Y. K., & Deming, D. 2005, *ApJ*, 632, 1122, [ADS](#), [astro-ph/0504212](#)
- Sharp, C. M., & Burrows, A. 2007, *ApJS*, 168, 140, [ADS](#), [astro-ph/0607211](#)
- Showman, A. P., Fortney, J. J., Lian, Y., Marley, M. S., Freedman, R. S., Knutson, H. A., & Charbonneau, D. 2009, *ApJ*, 699, 564, [ADS](#), [0809.2089](#)
- Stevenson, K. B. et al. 2012, *ApJ*, 754, 136, [ADS](#), [1108.2057](#)
- Stevenson, K. B. et al. 2010, *Nature*, 464, 1161, [ADS](#), [1010.4591](#)
- Taylor, J., Parmentier, V., Irwin, P. G. J., Aigrain, S., Lee, E. K. H., & Krissansen-Totton, J. 2020, *MNRAS*, 493, 4342, [ADS](#), [2002.00773](#)
- Tennyson, J. et al. 2016, *Journal of Molecular Spectroscopy*, 327, 73, [ADS](#), [1603.05890](#)
- ter Braak, C. J. F. 2006, *Statistics and Computing*, 16, 239
- ter Braak, C. J. F., & Vrugt, J. A. 2008, *Statistics and Computing*, 18, 435
- Virtanen, P. et al. 2020, *Nature Methods*, 17, 261, [ADS](#), [1907.10121](#)
- Waldmann, I. P., Tinetti, G., Rocchetto, M., Barton, E. J., Yurchenko, S. N., & Tennyson, J. 2015, *ApJ*, 802, 107, [ADS](#), [1409.2312](#)
- Yip, K. H., Changeat, Q., Edwards, B., Morvan, M., Chubb, K. L., Tsiaras, A., Waldmann, I. P., & Tinetti, G. 2021, *AJ*, 161, 4, [ADS](#), [2009.10438](#)
- Yurchenko, S. N., & Tennyson, J. 2014, *MNRAS*, 440, 1649, [ADS](#), [1401.4852](#)
- Zhang, M., Chachan, Y., Kempton, E. M. R., & Knutson, H. A. 2019, *PASP*, 131, 034501, [ADS](#), [1811.11761](#)

Appendix

A. Analysis of *Spitzer* Data

The *Spitzer Space Telescope* (warm-mission) obtained four transit light curves of HAT-P-11b (PI Deming, program ID 80128) using the IRAC instrument: two visits at 3.6 μm (2011 Jul 07 and Aug 15) and two visits at 4.5 μm (2011 Aug 05 and Aug 29). The telescope observed in sub-array mode with a cadence of 0.4 s. We re-analyzed these light curves with our Photometry for Orbits, Eclipses, and Transits (POET) pipeline (Stevenson et al. 2010, 2012; Campo et al. 2011; Nymeyer et al. 2011; Cubillos et al. 2013, 2014).

The POET analysis started by reading the *Spitzer* basic calibrated data (BCD) frames (*Spitzer* pipeline version 18.18.0). POET discarded bad pixels, determined the target position on the detector (fitting a circular, two-dimensional Gaussian function), and calculated aperture photometry to produce a raw light curve. For each event, we tested circular apertures with radii ranging from 1.75 to 4.0 pixels (in 0.25 pixel increments).

POET simultaneously modeled the out-of-transit system flux, eclipse curve, and telescope systematics with a Levenberg-Marquardt minimizer and a Markov-chain Monte Carlo routine. The *Spitzer* IRAC systematics include temporal and intra-pixel sensitivity variations (Charbonneau et al. 2005). We modeled the temporal systematic with a set of time-dependent “ramp” models (polynomial, exponential, and logarithmic functions, and combinations of them; Cubillos et al. 2013, 2014). We modeled the intra-pixel systematics with the Bi-Linearly Interpolated Sub-pixel Sensitivity (BLISS) map model (Stevenson et al. 2012). We used a Mandel & Agol (2002) model for the transit light curve. The transit model fit the planet-to-star radius ratio (R_p/R_s), transit midpoint time, cosine of inclination, and semi-major axis-to-stellar radius ratio (a/R_s). We adopted the same limb-darkening parameters as Fraine et al. (2014). We set the BLISS map grid size to the RMS of the frame-to-frame pointing jitter; changing the grid size did not impact the transit depth (Schwartz & Cowan 2017).

We determined the best-fitting aperture by minimizing the standard deviation of the normalized residuals (SDNR) between the data and the best-fitting model. Both 3.6 μm data sets showed a clear SDNR minimum at an aperture radius of 3.0 pixels. Similarly, both 4.5 μm data sets showed a clear SDNR minimum at 2.5 pixels. In all cases, the transit depth remained consistent (within 1σ) across the apertures.

We determined the best-fitting ramp model by minimizing the Bayesian Information Criterion (BIC). The value of BIC between two competing models (\mathcal{M}_1 and \mathcal{M}_2) indicates the fractional probability, $p(\mathcal{M}_2|D)$, of being the correct model (see Cubillos et al. 2014). Tables 3–6 show the best-fitting ramps for each data set.

At 3.6 μm , the rising-exponential ramp outperformed the other models in both visits. Since the second visit at 3.6 μm showed evidence of correlated noise (Fig. 8), we applied the time-averaging correction factor, and increased the data un-

Table 3. 3.6 μm Visit 1 - Ramp Model Fits

Ramp	R_p/R_s^a	ΔBIC	$p(\mathcal{M}_2 D)$
exponential	0.05835(19)	0.0	...
linear	0.05767(24)	2.3	0.24
quadratic	0.05839(35)	2.9	0.19
logarithmic	0.05766(22)	13.4	1.2×10^{-3}

Notes. ^a For this and the following tables, the value quoted in parentheses indicate the 1σ uncertainty corresponding to the least significant digits.

Table 4. 3.6 μm Visit 2 - Ramp Model Fits

Ramp	R_p/R_s	ΔBIC	$p(\mathcal{M}_2 D)$
exponential	0.05691(28)	0.0	...
exponential + linear	0.05687(26)	10.9	4.3×10^{-3}
logarithmic	0.05713(32)	20.2	4.1×10^{-5}
quadratic	0.05729(30)	105.8	1.1×10^{-23}

Table 5. 4.5 μm Visit 1 - Ramp Model Fits

Ramp	R_p/R_s	ΔBIC	$p(\mathcal{M}_2 D)$
no ramp	0.05798(33)	0.0	...
linear	0.05813(31)	3.0	0.18
quadratic	0.05807(36)	13.9	9.6×10^{-4}
exponential	0.05814(38)	14.0	9.1×10^{-4}

Table 6. 4.5 μm Visit 2 - Ramp Model Fits

Ramp	R_p/R_s	ΔBIC	$p(\mathcal{M}_2 D)$
no ramp	0.05814(35)	0.0	...
linear	0.05808(33)	10.9	4.3×10^{-3}
quadratic	0.05812(35)	21.9	1.8×10^{-5}
exponential	0.05814(29)	22.1	1.6×10^{-5}

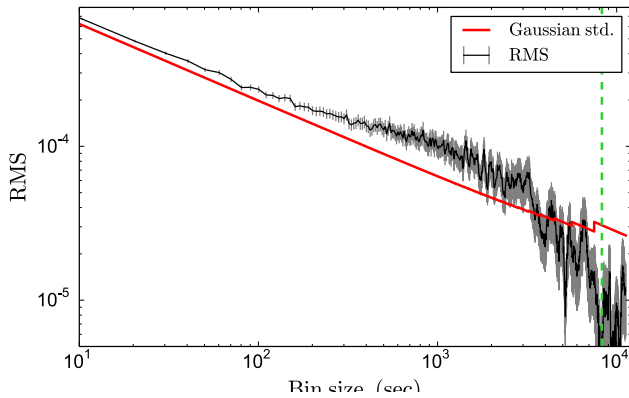


Figure 8. Fit residuals' rms (black curve with 1σ uncertainties) vs. bin size for the second visit at 3.6 μm . The red curve shows the expected rms for Gaussian (uncorrelated) noise. The green dashed vertical line marks the transit duration time.

4.5 μm , the no-ramp model outperformed the other models in both visits.

To obtain final transit depths we ran a joint fit combining all four events. In this fit, we shared the cosine of inclination and a/R_s parameters among all events. We also shared the R_p/R_s parameter between the events in the same wavelength band. Figure 9 shows the systematics-corrected light-curve data and joint best-fitting model. Table 7 summarizes the joint-fit model setup and results.

The *Spitzer* transit depth of POET and Fraine et al. (2014) are consistent to each other within 1σ . Furthermore, the depth uncertainties also agreed, suggesting that both reduction pipelines are statistically robust. This is relevant, considering that there have been disagreements when different groups analyze a same exoplanet light curve (Hansen et al. 2014).

certainties by a factor of 1.5 (see Cubillos et al. 2017). At

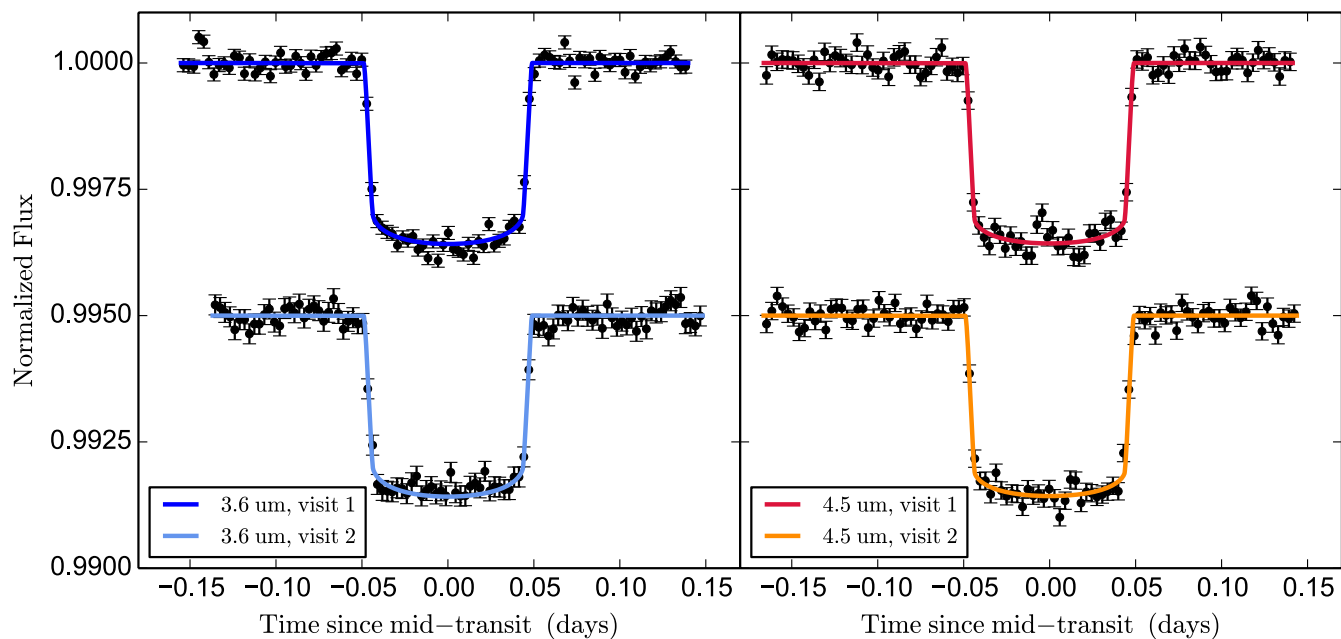


Figure 9. Normalized, systematics-corrected *Spitzer* HAT-P-11b transit light curves (black points) with the best-fitting models (colored solid curves). The error bars denote the 1σ uncertainties. For clarity, we binned the data points and vertically shifted the curves.

Table 7. HAT-P-11b Best Joint-fit Eclipse Light-curve Parameters

Parameter	3.6 μm (visit 1)	3.6 μm (visit 2)	4.5 μm (visit 1)	4.5 μm (visit 2)
Mean x position (pix)	14.91	14.89	14.61	14.74
Mean y position (pix)	15.13	15.12	15.06	15.02
x -position consistency ^a (pix)	0.004	0.005	0.012	0.010
y -position consistency ^a (pix)	0.011	0.006	0.005	0.004
Aperture photometry radius (pixels)	3.0	3.0	2.5	2.5
System flux F_s (μJy)	469650(17)	468700(17)	285075(5)	285511(5)
Transit midpoint (MJD _{UTC}) ^b	5749.63662(12)	5788.73918(20)	5778.96328(15)	5803.40230(17)
Transit midpoint (MJD _{TDB}) ^b	5749.63738(12)	5788.73994(20)	5778.96404(15)	5803.40306(17)
Transit duration (t_{4-1} , hrs)	2.351(4)	2.351(4)	2.351(4)	2.351(4)
R_p/R_s	0.05791(22)	0.05791(22)	0.05808(25)	0.05808(25)
$\cos(i)$ (deg)	89.52(12)	89.52(12)	89.52(12)	89.52(12)
a/R_s	16.67(8)	16.67(8)	16.67(8)	16.67(8)
Limb-darkening coefficient, c_1	0.5750	0.5750	0.6094	0.6094
Limb-darkening coefficient, c_2	-0.3825	-0.3825	-0.7325	-0.7325
Limb-darkening coefficient, c_3	0.3112	0.3112	0.7237	0.7237
Limb-darkening coefficient, c_4	-0.1099	-0.1099	-0.2666	-0.2666
Ramp equation ($R(t)$)	Rising exponential	Rising exponential	None	None
Ramp, exponential term (t_0)	-13.7(5.2)	29.8(3.6)
Ramp, exponential term (r_1)	-18.3(4.0)	11.5(2.2)
Number of free parameters ^c	7	7	5	5
Total number of frames	62592	62592	62592	62592
Frames used ^d	57999	56150	60962	62229
Rejected frames (%)	7.34	10.29	2.60	0.58
BIC	206185.0	206185.0	206185.0	206185.0
SDNR	0.0031105	0.0031215	0.0042606	0.0042751
Uncertainty scaling factor	0.980	1.477	1.083	1.086
Photon-limited S/N (%)	85.3	57.0	85.9	85.6

Notes. ^a rms frame-to-frame position difference.

^b MJD = BJD - 2,450,000.

^c In the individual fits.

^d We exclude frames during instrument/telescope settling, for insufficient points at a given BLISS bin, and for bad pixels in the photometry aperture.